

Extracting the Strain Matrix and Twist Angle from the Moiré Superlattice in van der Waals Heterostructures

Dorri Halbertal,* Sara Shabani, Abhay N. Passupathy, and D. N. Basov



Cite This: ACS Nano 2022, 16, 1471–1476



Read Online

ACCESS |

Metrics & More

Article Recommendations

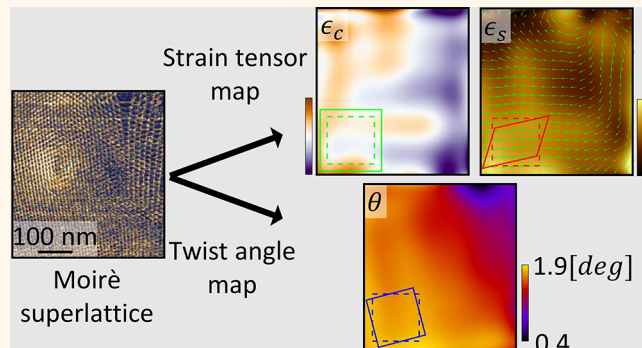
Supporting Information

ABSTRACT: When two atomic layers are brought into contact at a relative twist angle, a large-scale pattern, called a moiré superlattice, emerges due to the (angular or lattice) mismatch between the layers. This has profound consequences in terms of the Hamiltonian of the system but was also considered in several publications as a means to extract the local strain tensor. While extracting the twist angle based on knowledge of the periodicity of the moiré is trivial in the case of a regular moiré pattern, in many examples in the literature, that is not the case. In particular, extracting the strain tensor and twist angle maps from a spatially varying moiré pattern is not straightforward. This article aims to provide a practical tool to extract the strain tensor and twist angle from an experimentally observable pattern. It further addresses the limitation of any such approach in the absence of additional experimental information beyond the moiré superlattice pattern.

KEYWORDS: moiré superlattice, strain field, nanoimaging, scanning probe microscopy, vdW materials

The moiré superlattice generated by a lattice or twist-related mismatch has generated much interest in the past few years. Various papers have discussed the possibility of strain tensor extraction from the observable moiré spatial pattern using different imaging techniques including scanning tunneling microscopy (STM),^{1–5} piezoresponce force microscopy (PFM),^{6,7} conductive atomic force microscopy (CAFM),⁸ scattering-type scanning near-field optical microscopy (s-SNOM),^{9–12} microwave impedance microscopy,¹³ and transmission electron microscopy (TEM)-based techniques.^{14–17} Whether the strain is deliberate or spontaneously formed, it may strongly affect the system under study¹⁸ and, in particular, the moiré potential.^{1,19} While the notion of strain extraction has been discussed before, there is a need for a more standardized approach to the problem. Furthermore, the limitations of what can be extracted from the moiré superlattice pattern should be clear when making such an attempt.

This work aims to provide a detailed derivation of the problem, offer a practical tool for strain and twist angle extraction from an experimentally observed pattern, as well as lay out the limitation of such an approach. The twist angle and strain map extraction scheme is demonstrated in Figure 1: starting from a raw STM topography of a MoSe₂/WSe₂



heterostructure (Figure 1a), through processing (Figure 1b), and finally the extraction of maps of the twist angle (Figure 1c) and the strain tensor (Figure 1d,e). The details of the procedure are discussed in this paper as follows: we start by presenting the assumptions and the derivation of the strain extraction scheme. Then we present results covering a broad span of scenarios in the moiré superlattice parameter space and extend the scheme to a spatially varying moiré pattern, as in the example of Figure 1. Finally, we discuss inherent limitations of the approach. We hope this short dedicated article will be useful for analysis of experiments in the field of twisted van der Waals heterostructures (a code is provided as part of the Supporting Information) as well as prevent ambiguity by creating a standard for moiré-based strain extraction.

Received: November 4, 2021

Accepted: December 30, 2021

Published: January 4, 2022



ACS Publications

© 2022 American Chemical Society

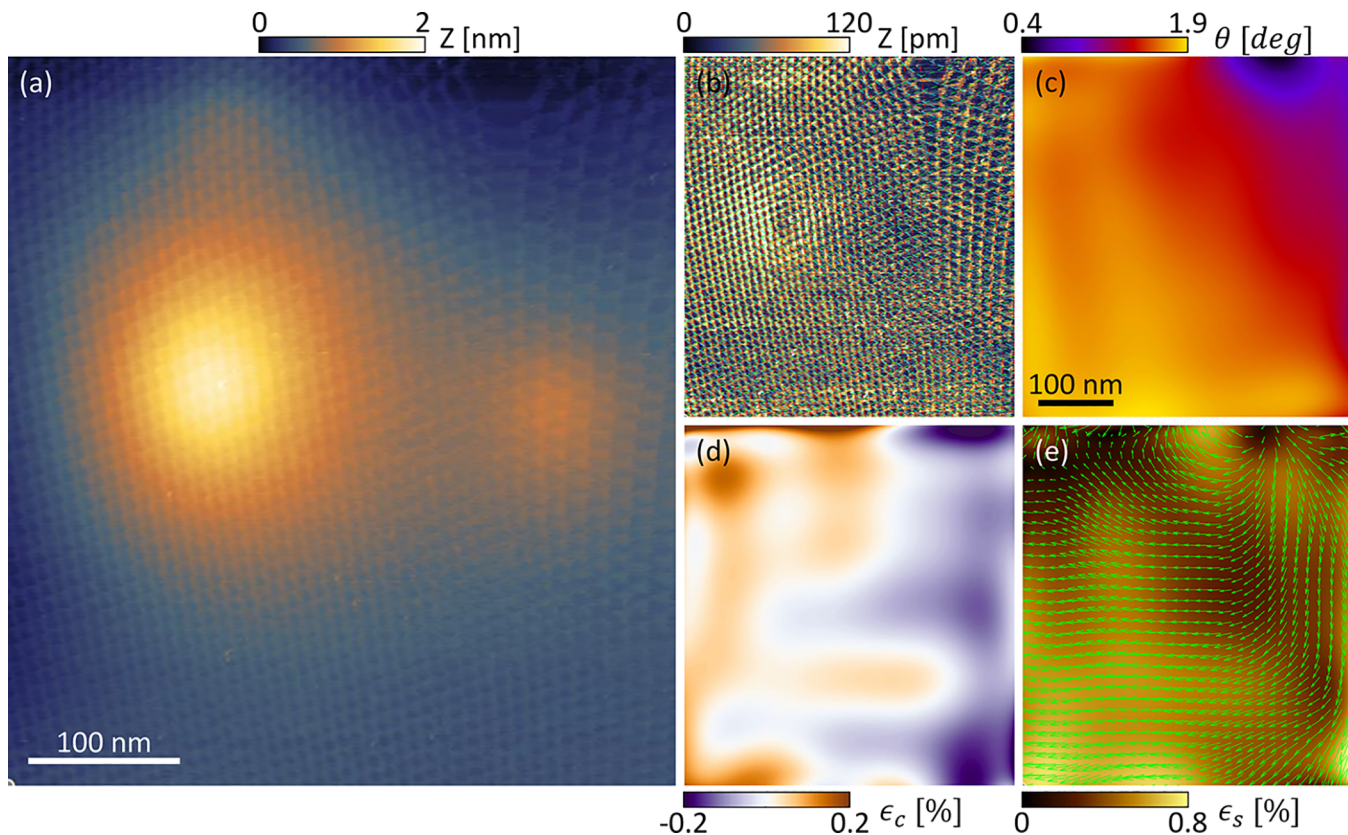


Figure 1. Strain and twist angle fields extraction from a spatially varying moiré superlattice map. (a) STM topography map of a twisted MoSe₂/WSe₂ heterostructure. Two bubbles cause a large-scale topography features over which the moiré superlattice is apparent. (b) Data of (a) after background subtraction (see Methods) to highlight moiré). Overlaid over the data are the integer value registry contours for I (red), J (green), and $I + J$ (cyan), as produced by polynomial fits of the $I(r)$ and $J(r)$ functions. (c–e) Using eq 9 and a common choice of ϕ_0 , the maps for θ (c), the compression strain ϵ_c (d), and the shear strain ϵ_s (e) were extracted. The vector field $\epsilon_s(\cos \gamma, \sin \gamma)$ is overlaid on top of the map of ϵ_s in (e). Panels c–e share a scale bar. The total strain minimization yielded $\phi_0 = -65.6^\circ$.

RESULTS AND DISCUSSION

Strain Extraction Scheme. We assume two hexagonal lattices, layer 1 and layer 2, with unit cell spacing α_1 and α_2 , respectively. We assume layer 2 is twisted by an unknown angle θ relative to layer 1 (see Figure 2). We further assume that the emerging moiré superlattice pattern from these two lattices is characterized by only two lattice vectors ν_1 and ν_2 ,

where $\nu_j = \lambda_j \begin{pmatrix} \cos \phi_j \\ \sin \phi_j \end{pmatrix}$ for $j = 1, 2$. In this regard, we do not

consider the sub-moiré details of the structure but focus solely on the moiré unit cell size. The moiré pattern reflects the stacking configuration between the two atomic layers across the twisted interface. While a strain field in each layer clearly affects the resulting moiré pattern, there is not enough information in the pattern itself to decouple the strain tensor of each layer individually. However, the moiré pattern is strongly affected by the heterostrain, the relative strain between the two layers, in contrast with the common strain of the two layers. The latter will only affect the pattern up to the common strain size itself and is therefore restricted to below 2% before solitons start to form.²⁰ This is because heterostrain affects the incommensurability of the two lattices whereas common strain does not. Here, we will neglect the common strain term and, for simplicity, assume layer 1 (the substrate) to be rigid. In such a case, the heterostrain is completely encoded in the displacement field for layer 2, marked by $\mathbf{u}_2(r)$. Whereas layer

1 cannot, in general, be regarded as rigid, this approach will still provide a good proxy for the heterostrain responsible for producing the observed moiré pattern. Furthermore, as we do not consider the sub-moiré details, we disregard the effects of atomic relaxation, generating additional strain within a given moiré cell (see refs 1 and 9 for such considerations). We therefore assume the strain and twist angle to be slowly varying across the moiré length scale and write the displacement field locally as $\mathbf{u}_2(r) = \hat{\Sigma}r$. We attempt to extract the tensor $\hat{\Sigma}$ from the observed pattern (as captured by the observables ν_1 and ν_2) and the prior knowledge of α_1 and α_2 . As derived below, the tensor $\hat{\Sigma}$ satisfying the above requirements is not unique, but one can still extract useful information from the observed pattern and reach a unique solution by prior knowledge of the crystallographic orientation of the substrate.

The vector connecting neighboring A sites is oriented at an angle ϕ_0 relative to the x -axis. We define two unit vectors:

$$\mathbf{b}_1 = \begin{pmatrix} \cos \phi_0 \\ \sin \phi_0 \end{pmatrix}, \quad \mathbf{b}_2 = \begin{pmatrix} \cos\left(\phi_0 + \frac{\pi}{3}\right) \\ \sin\left(\phi_0 + \frac{\pi}{3}\right) \end{pmatrix} \quad (1)$$

We arbitrarily set the origin on one of the A sites of layer 1. The A sites of layer 1 will therefore be at the following locations:

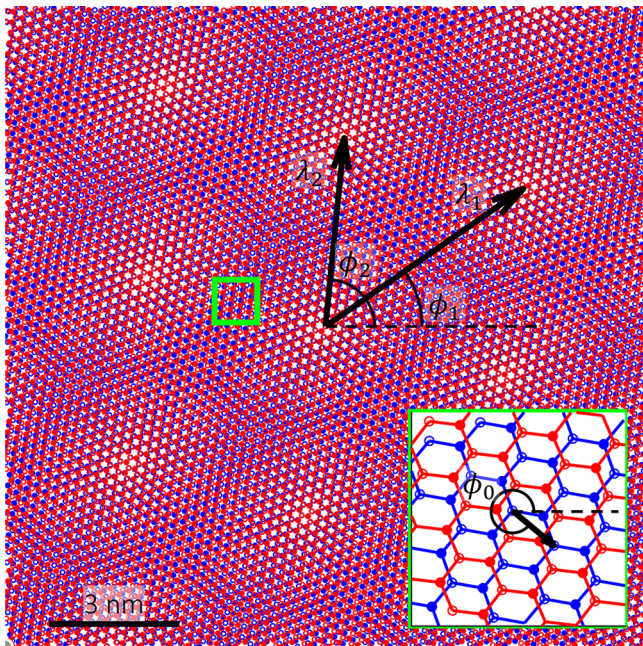


Figure 2. Moiré superlattice pattern and scheme notations. Two hexagonal lattices, with unit cell spacing α_1 (lattice 1, blue) and α_2 (lattice 2, red) are twisted by θ relative to one another. ϕ_0 defines the lattice orientation of layer 1 (see inset) connecting two A sites. The emerging moiré superlattice pattern is characterized by vectors $\lambda_1(\cos \phi_1, \sin \phi_1)$ and $\lambda_2(\cos \phi_2, \sin \phi_2)$. Inset: Zoom-in image of the region marked by the green rectangle. Atoms of layers 1 and 2 are marked by blue and red circles, respectively. A and B sites are marked by empty and full circles, respectively. In this example, $\phi_0 = -40^\circ$, $\alpha_1 = 0.251$ nm, $\alpha_2 = 0.247$ nm, $\theta = 3^\circ$. A shear strain term with $\epsilon_c = 1\%$, $\gamma = 0^\circ$ was added.

$$\mathbf{r}_A^{(1)}(i_1, j_1) = \alpha_1 [\mathbf{b}_1 \mathbf{b}_2] \begin{pmatrix} i_1 \\ j_1 \end{pmatrix}$$

For integer values i_1 and j_1 . The A sites of layer 2 will be at (for integer values i_2 and j_2)

$$\mathbf{r}_A^{(2)}(i_2, j_2) = R_\theta \alpha_2 [\mathbf{b}_1 \mathbf{b}_2] \begin{pmatrix} i_2 \\ j_2 \end{pmatrix} + \hat{\Sigma} \mathbf{r} + \Delta \mathbf{r}$$

where $R_\theta = \begin{pmatrix} \cos \theta & -\sin \theta \\ \sin \theta & \cos \theta \end{pmatrix}$ is a rotation matrix by angle θ in two dimensions and $\Delta \mathbf{r}$ is some global displacement (will be later discarded). We define $1 + \delta = \frac{\alpha_2}{\alpha_1}$, $\alpha = \alpha_2$. From the above definitions, we can express the stacking configuration at a point \mathbf{r} as a 2D vector where integer values correspond to A-A stacking:

$$\begin{pmatrix} i_2 - i_1 \\ j_2 - j_1 \end{pmatrix} = \frac{1}{\alpha} [\mathbf{b}_1 \mathbf{b}_2]^{-1} (R_{-\theta}(I_2 - \hat{\Sigma}) \mathbf{r} - (1 + \delta) \mathbf{r} - R_{-\theta} \Delta \mathbf{r})$$

where I_2 is the identity matrix in two dimensions. Next, we can write an expression for our observable $[\mathbf{v}_1 \mathbf{v}_2]$:

$$[\mathbf{v}_1 \mathbf{v}_2] = \alpha (R_{-\theta}(I_2 - \hat{\Sigma}) - (1 + \delta) I_2)^{-1} [\mathbf{b}_1 \mathbf{b}_2]$$

If we assume the knowledge of θ and ϕ_0 , we can easily rewrite the last expression as

$$\hat{\Sigma} = I_2 - R_\theta (\alpha [\mathbf{b}_1 \mathbf{b}_2] [\mathbf{v}_1 \mathbf{v}_2]^{-1} + (1 + \delta) I_2) \quad (2)$$

As we want to eliminate any twist-related terms from the matrix $\hat{\Sigma}$ such that all such terms will be incorporated in θ , we can force $\hat{\Sigma}_{1,2} = \hat{\Sigma}_{2,1}$ by tuning the value of θ . It is straightforward to show that such a condition is achieved when

$$e^{i\theta(\phi_0)} = \frac{1}{R(\phi_0)} (x(\phi_0) + iy(\phi_0)) \quad (3)$$

where

$$x(\phi_0) \equiv x_0 + r_- \cos(\Delta\phi_{0,-} - \phi_0) \quad (4a)$$

$$y(\phi_0) \equiv r_- \sin(\Delta\phi_{0,-} - \phi_0) \quad (4b)$$

$$R(\phi_0) \equiv \sqrt{x(\phi_0)^2 + y(\phi_0)^2} \quad (4c)$$

and

$$\Delta\phi \equiv \phi_2 - \phi_1 \quad (5a)$$

$$x_0 \equiv \frac{2(1 + \delta)}{\alpha} \lambda_1 \lambda_2 \sin \Delta\phi \quad (5b)$$

$$r_\pm \equiv \sqrt{\lambda_1^2 + \lambda_2^2 - 2\lambda_1 \lambda_2 \cos\left(\Delta\phi \mp \frac{\pi}{3}\right)} \quad (5c)$$

$$e^{i\Delta\phi_{0,\pm}} \equiv \frac{i}{r_\pm} (\lambda_1 e^{i(\phi_1 \pm \frac{\pi}{3})} - \lambda_2 e^{i\phi_2}) \quad (5d)$$

As $\hat{\Sigma}$ is a symmetric 2×2 matrix, it can be written as $\hat{\Sigma} = \epsilon_c I_2 + \epsilon_s \begin{pmatrix} \cos \gamma & \sin \gamma \\ \sin \gamma & -\cos \gamma \end{pmatrix}$, where ϵ_c and ϵ_s are the isotropic compression strain and the shear strain terms, respectively, and γ is the strain tensor angle. It is straightforward to show that the shear strain, ϵ_s , is in fact independent of ϕ_0 and equals

$$\epsilon_s = \frac{\alpha \sqrt{\lambda_1^2 + \lambda_2^2 - 2\lambda_1 \lambda_2 \cos\left(\Delta\phi - \frac{\pi}{3}\right)}}{2\lambda_1 \lambda_2 \sin(\Delta\phi)} \quad (6)$$

Similarly, one can derive an expression for the compression strain, ϵ_c , and the strain angle, γ :

$$\epsilon_c(\phi_0) = 1 - \frac{(1 + \delta)}{x_0} R(\phi_0) \quad (7)$$

$$e^{i\gamma(\phi_0)} = e^{i(\theta(\phi_0) + \Delta\phi_{0,+} + \phi_0 + \pi)} \quad (8)$$

Unlike ϵ_s , the parameters θ , ϵ_c , and γ depend on the substrate lattice orientation ϕ_0 . It is therefore important to note that for a given experimental configuration there is not a unique solution of twist angle and strain tensor that would generate it. In fact, Figure 3a,b presents a full range of such solutions, each with its own value of ϕ_0 . If ϕ_0 is known in addition to the moiré pattern, then the solution is unique. In most experiments, that is not the case, and one is forced to make additional assumptions to effectively choose among the available solutions. However, as seen in Figure 3b, the compression strain ϵ_c varies considerably as a function of ϕ_0 covering extreme strain values, which do not necessarily make physical sense. One approach can therefore be to choose ϕ_0 as the value resulting in minimal ϵ_c^2 . In the following section, we

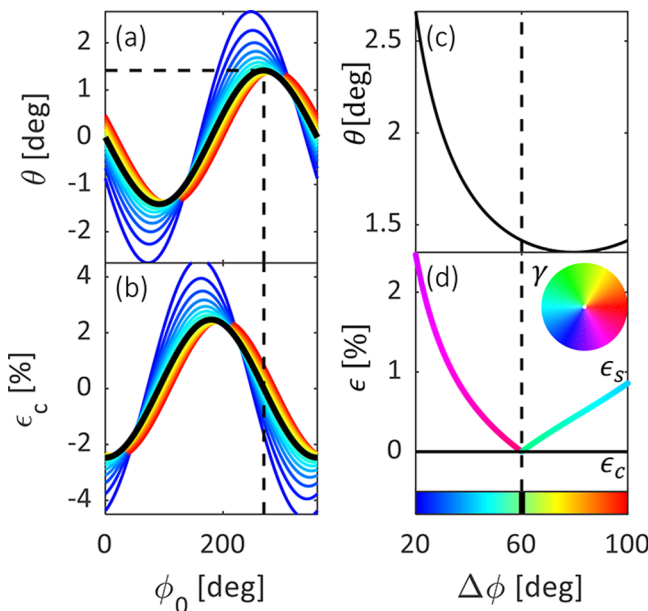


Figure 3. Effect of angle between moiré vectors on extracted strain tensor and twist angle. (a,b) Extracted parameters as a function of ϕ_0 for different values of $\Delta\phi$. (a) Extracted twist angle. (b) Extracted compression strain, ϵ_c . (c,d) Extracted parameters by choosing ϕ_0 that minimizes ϵ_c^2 : (c) twist angle and (d) compression (black line) and shear strain (colored according to the color-wheel capturing the shear strain angle γ , as defined in the text). In all cases, $\alpha_1 = 0.247$ nm, $\lambda_1 = \lambda_2 = 10$ nm, $\phi_1 = 0^\circ$. The $\Delta\phi$ value in (a,b) is indicated by color according to the color map in (d). The dashed lines indicate the zero strain values.

will explore this approach and also extend it to the case where the moiré superlattice is nonuniform.

Examples of Scheme Application. In this section, we explore the strain extraction scheme. In all cases, we consider a layer of graphene with $\alpha_2 = 0.247$ nm and arbitrarily set $\phi_1 = 0^\circ$. We will consider a system without mismatch, where $\alpha_1 = \alpha_2$ and also a mismatched system. Figure 3 explores the effect of varying the angle between the two moiré vectors, marked as $\Delta\phi$. Figure 3a,b shows the extracted twist angle (Figure 3a) and total strain (Figure 3b) as a function of ϕ_0 . As expected, at $\Delta\phi = 60^\circ$ (bold black line), the resulting θ value when the total strain is zero is in agreement with the value predicted by $\lambda = \frac{\alpha}{2 \sin \theta / 2}$ (dashed black line). Next we follow the proposed choice of ϕ_0 that minimizes the total strain, and plot as a function of $\Delta\phi$ the resulting twist angle (Figure 3c) and strain tensor as captured by the isotropic compression strain and the shear strain terms, ϵ_c and ϵ_s , respectively, as well as the strain tensor angle, γ (Figure 3d). The compression strain is identically zero, whereas the shear strain sharply changes its orientation across $\Delta\phi = 60^\circ$, as captured by the color change of ϵ_s in Figure 3d. This is a result of the poor definition of $\Delta\phi_+$ in eq 5a when $\epsilon_s = 0$. Next, we extend the analysis to a lattice-mismatched system and explore various moiré pattern scenarios over the two-dimensional plane of $\Delta\phi$ and λ_2 while keeping λ_1 fixed (Figure 4). In each point, ϕ_0 was chosen as to minimize ϵ_c^2 . For some region in the parameter space, the condition $\epsilon_c = 0$ cannot be achieved, resulting in a sharp drop in the extracted twist angle (see region marked by dashed curve in Figure 4a,b). The extracted shear strain grows away from the $\Delta\phi = 60^\circ$, $\lambda_1 = \lambda_2$ point (Figure 4c) and circles that point (Figure 4d).

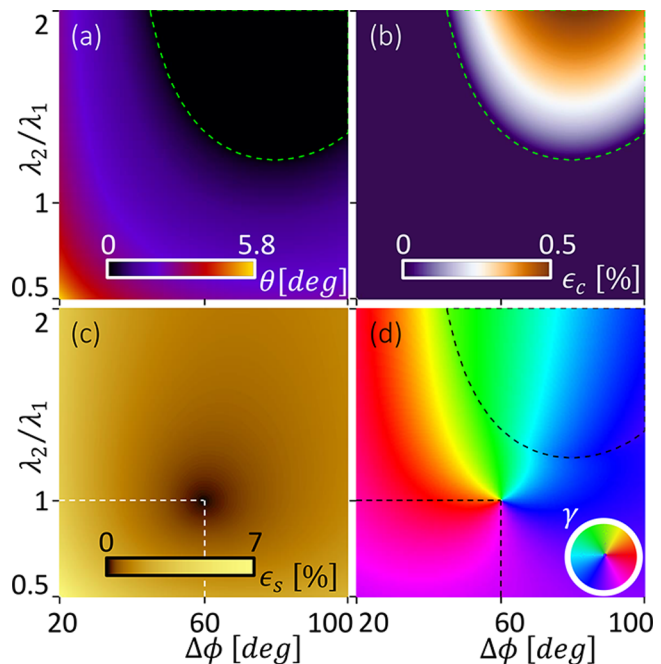


Figure 4. Effect of length ratio and angle between moiré vectors on extracted strain tensor and twist angle for a mismatched system. (a) Extracted twist angle, (b) compression strain ϵ_c , (c) shear strain ϵ_s , and (d) shear strain angle γ (colored according to the color wheel in the inset), all as a function of $\Delta\phi = \phi_2 - \phi_1$ and λ_2/λ_1 . At every point ϕ_0 was chosen as to minimize ϵ_c^2 . ϵ_c is identically zero except for the region marked by dashed frame in (a,b,d). In all cases, $\alpha_1 = 0.255$ nm and $\alpha_2 = 0.247$ (giving a mismatch of $\delta = -0.03$), $\lambda_1 = 10$ nm, and $\phi_1 = 0^\circ$.

The strain and twist angle extraction scheme can be easily extended to a case of a spatially varying moiré pattern, such that $[\mathbf{v}_1 \mathbf{v}_2]$ is a function of space. Such an example was considered previously in Figure 1. Figure 1a presents an STM topography map of a twisted WSe₂/MoSe₂ heterostructure. Due to the existence of two bubbles, there are large-scale topographic features affecting the strain field. Figure 1b presents the same data after background subtraction (see Methods) to enhance the moiré superlattice pattern. One can define the moiré registry functions $I(\mathbf{r})$ and $J(\mathbf{r})$ such that each function returns an integer value across a contour crossing A–A stacking (Figure 1b, where the red curves are integer I contours and the green curves are integer J contours). Following such a definition, and assuming $\theta(\mathbf{r})$ and $\hat{\Sigma}(\mathbf{r})$ are varying slowly over the moiré scale, one can define the vector function of the moiré vectors as

$$[\mathbf{v}_1(\mathbf{r}) \mathbf{v}_2(\mathbf{r})] \equiv \begin{bmatrix} \nabla I(\mathbf{r}) \\ \nabla J(\mathbf{r}) \end{bmatrix}^{-1} \quad (9)$$

This approach to the spatially varying moiré pattern resembles the Lawler–Fujita algorithm,^{21,22} where one attempts to correct atomic-scale images for drift by constructing a large-scale displacement field. This displacement field projects the perturbed observation to a perfectly periodic structure. Here, the moiré pattern can be thought of as the drift-perturbed pattern, and the strain field is related to the correcting displacement field. We can therefore follow the extraction scheme on a point-by-point basis. The only question left is the choice of $\phi_0(\mathbf{r})$. As before, without additional information, we

assume ϕ_0 to be uniform across the image and set it such that $\epsilon_c(r)^2$ integrated over the image is minimized. The resulting maps of the twist angle, compression strain, and shear strain are plotted in Figure 1c–e.

Scheme Limitations. The strain and twist angle extraction scheme presented here is rather straightforward. However, one should keep in mind that while minimizing the extracted strain as a guide for choice of ϕ_0 is logical, the extracted twist angle and strain tensor are not guaranteed to agree with the actual experimental configuration (see Supporting Information for further discussion). If there is additional experimental information, it should be incorporated into choosing ϕ_0 . For instance, if one attempts to extract the strain map from a spatially varying moiré superlattice, one may consider taking a common ϕ_0 value rather than minimizing ϵ_c^2 at every location. Such an approach is demonstrated in the experimental example of Figure 1. This example highlights another limitation of the extraction scheme, as the bubbles appearing in the topography map of Figure 1a clearly create strain, which is not reflected in the twist angle (Figure 1c) or strain tensor map (Figure 1d,e) in an obvious way. This is because the bubbles are clearly trapped underneath the heterostructure. These bubbles exert a common strain on both layers, therefore deviating from our assumptions of a rigid substrate.

Another limit to consider is the very small twist angle limit for homobilayer structures. In such cases, the strain may change on scales comparable or even smaller than the moiré superlattice.^{9,12,13,23} In such cases, the moiré unit cell is no longer a sufficiently good proxy of the strain field, and one may need to resort to more detailed mechanical relaxation calculations to extract the strain map.⁹

CONCLUSIONS

In this short paper, we have presented a scheme to extract the strain tensor and the twist angle from the experimentally observable moiré superlattice. While the derivation is straightforward, with several variations considered to some extent in recent publications, we thought it valuable to standardize the approach by offering a recipe as well as highlighting the limitations of the approach, as reflected in the uncertainty analysis. We further provide a Matlab code that can be used as is to extract the strain tensor and twist angle within the presented assumptions.

METHODS

Scanning Tunneling Microscopy Measurements. The presented topographies in this work were carried out in a room temperature and ultrahigh vacuum system. The topographies were taken at constant current and bias set-points using a feedback loop. The set-points used for Figure 1a,b were $V = -1.7$ V and $I = 100$ pA.

Sample Fabrication. WSe₂ and MoSe₂ monolayers were exfoliated from high-quality single crystals (the bulk crystals of MoSe₂ and WSe₂ were grown by the self-flux method).²⁴ The stacking method is based on the dry transfer technique.²⁵ Polypropylene carbonate was used to pick up a 50 nm thick hexagonal boron nitride flake and a few layers of graphite. Then WSe₂ and MoSe₂ monolayers were picked up subsequently in a way that the twist angle between two layers was 1.7°. Prior to the stacking, the relative orientation between two monolayers was extracted from second harmonic generation measurements to determine the rotation of the transfer stage, leading to a 1.7° twist angle. In the last step, the stack was flipped to a Si/SiO₂ substrate at 120 °C. The electrical contact from the graphite flake to the STM bias was made using microsoldering with Field's metal.²⁶

Strain Field Extraction for a Spatially Varying Moiré Superlattice Pattern. In the example of Figure 1, we explored the application of the strain tensor and twist angle extraction scheme to a spatially varying experimental case. At the basis of the implementation was the extraction of the registries indices $I(r)$ and $J(r)$ fields. The extraction was performed by manually sample registries of the moiré superlattice across the image. Then a high power ($n = 11$) two-dimensional polynomial fit. The moiré vectors field [$v_1(r)$ $v_2(r)$] was extracted using eq 9, where the gradients of the registry fields were taken analytically, as the gradients of the two-dimensional polynomial fit.

Background Subtraction Scheme. The map of Figure 1b was leveled using the “revolve sphere” method with a radius of $r = 20$ nm in Gwyddion—the free SPM data analysis software, performed over the raw data presented in Figure 1a. Data are leveled by revolving a virtual “sphere” over the data and treating the envelope of the sphere as a background. This results in the removal of features on a considerably larger scale than the sphere radius.

ASSOCIATED CONTENT

SI Supporting Information

The Supporting Information is available free of charge at <https://pubs.acs.org/doi/10.1021/acsnano.1c09789>.

A discussion about the limitation of the compressive strain minimization approach for estimating the lattice orientation, which presents an extreme case in which in the absence of knowledge of the lattice orientation, the estimation will fail, and the strain extraction scheme will fail, as well (PDF)

Matlab code that includes an implementation of the strain extraction scheme (PDF)

AUTHOR INFORMATION

Corresponding Author

Dorri Halbertal – Department of Physics, Columbia University, New York, New York 10027, United States;
ORCID.org/0000-0002-1665-0724; Email: dorrihal@gmail.com

Authors

Sara Shabani – Department of Physics, Columbia University, New York, New York 10027, United States

Abhay N. Passupathy – Department of Physics, Columbia University, New York, New York 10027, United States;
ORCID.org/0000-0002-2744-0634

D. N. Basov – Department of Physics, Columbia University, New York, New York 10027, United States

Complete contact information is available at:
<https://pubs.acs.org/10.1021/acsnano.1c09789>

Notes

The authors declare no competing financial interest.

ACKNOWLEDGMENTS

This work is supported by the Programmable Quantum Materials (Pro-QM) programme at Columbia University, an Energy Frontier Research Center established by the Department of Energy (Grant No. DE-SC0019443). The strain extraction scheme development was supported by the U.S. Department of Energy (DOE), Office of Science, Basic Energy Sciences (BES), under Award DE-SC0018426 (D.H. and D.N.B.). STM experiments were supported by the Air Force Office of Scientific Research via Grant No. FA9550-16-1-0601 (S.S. and A.N.P.). D.H. was supported by a grant from the

Simons Foundation (579913). D.N.B. is the Vannevar Bush Faculty Fellow ONR-VB: N00014-19-1-263 and the Moore Investigator in Quantum Materials EPIQS 9455.

REFERENCES

- (1) Shabani, S.; Halbertal, D.; Wu, W.; Chen, M.; Liu, S.; Hone, J.; Yao, W.; Basov, D. N.; Zhu, X.; Pasupathy, A. N. Deep Moiré Potentials in Twisted Transition Metal Dichalcogenide Bilayers. *Nat. Phys.* **2021**, *17*, 720–725.
- (2) Benschop, T.; de Jong, T. A.; Stepanov, P.; Lu, X.; Stalman, V.; van der Molen, S. J.; Efetov, D. K.; Allan, M. P. Measuring Local Moiré Lattice Heterogeneity of Twisted Bilayer Graphene. *Physical Review Research* **2021**, *3*, 013153.
- (3) Woods, C. R.; et al. Commensurate-Incommensurate Transition in Graphene on Hexagonal Boron Nitride. *Nat. Phys.* **2014**, *10*, 451–456.
- (4) Jiang, Y.; Mao, J.; Duan, J.; Lai, X.; Watanabe, K.; Taniguchi, T.; Andrei, E. Y. Visualizing Strain-Induced Pseudomagnetic Fields in Graphene Through an hBN Magnifying Glass. *Nano Lett.* **2017**, *17*, 2839–2843.
- (5) Shi, H.; Zhan, Z.; Qi, Z.; Huang, K.; van Veen, E.; Silva-Guillén, J. A.; Zhang, R.; Li, P.; Xie, K.; Ji, H.; Katsnelson, M. I.; Yuan, S.; Qin, S.; Zhang, Z. Large-Area, Periodic, and Tunable Intrinsic Pseudo-Magnetic Fields in Low-Angle Twisted Bilayer Graphene. *Nat. Commun.* **2020**, *11*, 371.
- (6) Bai, Y.; et al. Excitons in Strain-Induced One-Dimensional Moiré Potentials at Transition Metal Dichalcogenide Heterojunctions. *Nat. Mater.* **2020**, *19*, 1068–1073.
- (7) McGilly, L. J.; et al. Visualization of Moiré Superlattices. *Nat. Nanotechnol.* **2020**, *15*, 580–584.
- (8) Rosenberger, M. R.; Chuang, H.-J.; Phillips, M.; Oleshko, V. P.; McCreary, K. M.; Sivaram, S. V.; Hellberg, C. S.; Jonker, B. T. Twist Angle-Dependent Atomic Reconstruction and Moiré Patterns in Transition Metal Dichalcogenide Heterostructures. *ACS Nano* **2020**, *14*, 4550–4558.
- (9) Halbertal, D.; Finney, N. R.; Sunku, S. S.; Kerelsky, A.; Rubio-Verdu, C.; Shabani, S.; Xian, L.; Carr, S.; Chen, S.; Zhang, C.; Wang, L.; Gonzalez-Acevedo, D.; McLeod, A. S.; Rhodes, D.; Watanabe, K.; Taniguchi, T.; Kaxiras, E.; Dean, C. R.; Hone, J. C.; Pasupathy, A. N.; Kennes, D. M.; Rubio, A.; Basov, D. N. Moiré Metrology of Energy Landscapes in van der Waals Heterostructures. *Nat. Commun.* **2021**, *12*, 242.
- (10) Ni, G. X.; Wang, H.; Jiang, B. Y.; Chen, L. X.; Du, Y.; Sun, Z. Y.; Goldflam, M. D.; Frenzel, A. J.; Xie, X. M.; Fogler, M. M.; Basov, D. N. Soliton Superlattices in Twisted Hexagonal Boron Nitride. *Nat. Commun.* **2019**, *10*, 4360.
- (11) Chen, X.; et al. Moiré Engineering of Electronic Phenomena in Correlated Oxides. *Nat. Phys.* **2020**, *16*, 631–635.
- (12) Moore, S. L.; Ciccarino, C. J.; Halbertal, D.; McGilly, L. J.; Finney, N. R.; Yao, K.; Shao, Y.; Ni, G.; Sternbach, A.; Telford, E. J.; Kim, B. S.; Rossi, S. E.; Watanabe, K.; Taniguchi, T.; Pasupathy, A. N.; Dean, C. R.; Hone, J.; Schuck, P. J.; Narang, P.; Basov, D. N. Nanoscale Lattice Dynamics in Hexagonal Boron Nitride Moiré Superlattices. *Nat. Commun.* **2021**, *12*, 5741.
- (13) Lee, K.; Utama, M. I. B.; Kahn, S.; Samudrala, A.; Leconte, N.; Yang, B.; Wang, S.; Watanabe, K.; Taniguchi, T.; Altoe, M. V. P.; Zhang, G.; Weber-Bargioni, A.; Crommie, M.; Ashby, P. D.; Jung, J.; Wang, F.; Zettl, A. Ultrahigh-Resolution Scanning Microwave Impedance Microscopy of Moiré Lattices and Superstructures. *Science Advances* **2020**, *6*, eaax6212.
- (14) Yoo, H.; et al. Atomic and Electronic Reconstruction at the van der Waals Interface in Twisted Bilayer Graphene. *Nat. Mater.* **2019**, *18*, 448–453.
- (15) Alden, J. S.; Tsien, A. W.; Huang, P. Y.; Hovden, R.; Brown, L.; Park, J.; Muller, D. A.; McEuen, P. L. Strain Solitons and Topological Defects in Bilayer Graphene. *Proc. Natl. Acad. Sci. U. S. A.* **2013**, *110*, 11256–11260.
- (16) Kazmierczak, N. P.; Van Winkle, M.; Ophus, C.; Bustillo, K. C.; Carr, S.; Brown, H. G.; Ciston, J.; Taniguchi, T.; Watanabe, K.; Bediako, D. K. Strain Fields in Twisted Bilayer Graphene. *Nat. Mater.* **2021**, *20*, 956–963.
- (17) Weston, A.; et al. Atomic Reconstruction in Twisted Bilayers of Transition Metal Dichalcogenides. *Nat. Nanotechnol.* **2020**, *15*, 592–597.
- (18) Kennes, D. M.; Claassen, M.; Xian, L.; Georges, A.; Millis, A. J.; Hone, J.; Dean, C. R.; Basov, D. N.; Pasupathy, A. N.; Rubio, A. Moiré Heterostructures as Condensed-Matter Quantum Simulator. *Nat. Phys.* **2021**, *17*, 155–163.
- (19) Shimazaki, Y.; Schwartz, I.; Watanabe, K.; Taniguchi, T.; Kroner, M.; Imamoğlu, A. Strongly Correlated Electrons and Hybrid Excitons in a Moiré Heterostructure. *Nature* **2020**, *580*, 472–477.
- (20) Edelberg, D.; Kumar, H.; Shenoy, V.; Ochoa, H.; Pasupathy, A. N. Tunable Strain Soliton Networks Confine Electrons in van der Waals Materials. *Nat. Phys.* **2020**, *16*, 1097–1102.
- (21) Lawler, M. J.; Fujita, K.; Lee, J.; Schmidt, A. R.; Kohsaka, Y.; Kim, C. K.; Eisaki, H.; Uchida, S.; Davis, J. C.; Sethna, J. P.; Kim, E. A. Intra-Unit-Cell Electronic Nematicity of the High-T_c Copper-Oxide Pseudogap States. *Nature* **2010**, *466*, 347–351.
- (22) Gutiérrez, C.; Kim, C. J.; Brown, L.; Schiros, T.; Nordlund, D.; Lochocki, E. B.; Shen, K. M.; Park, J.; Pasupathy, A. N. Imaging Chiral Symmetry Breaking from Kekulé Bond Order in Graphene. *Nat. Phys.* **2016**, *12*, 950–958.
- (23) Sunku, S. S.; Halbertal, D.; Stauber, T.; Chen, S.; McLeod, A. S.; Rikhter, A.; Berkowitz, M. E.; Lo, C. F.; Gonzalez-Acevedo, D. E.; Hone, J. C.; Dean, C. R.; Fogler, M. M.; Basov, D. N. Hyperbolic Enhancement of Photocurrent Patterns in Minimally Twisted Bilayer Graphene. *Nat. Commun.* **2021**, *12*, 1641.
- (24) Edelberg, D.; et al. Approaching the Intrinsic Limit in Transition Metal Diselenides via Point Defect Control. *Nano Lett.* **2019**, *19*, 4371–4379.
- (25) Huang, Y.; Sutter, E.; Shi, N. N.; Zheng, J.; Yang, T.; Englund, D.; Gao, H. J.; Sutter, P. Reliable Exfoliation of Large-Area High-Quality Flakes of Graphene and Other Two-Dimensional Materials. *ACS Nano* **2015**, *9*, 10612–10620.
- (26) Girit, C. O.; Zettl, A. Soldering to a Single Atomic Layer. *Appl. Phys. Lett.* **2007**, *91*, 193512.